

Low-loss lateral micromachined switches for high frequency applications

A Q Liu¹, M Tang¹, A Agarwal² and A Alphones¹

¹ School of Electrical and Electronic Engineering, Nanyang Technological University, Nanyang Avenue, 639798, Singapore

² Institute of Microelectronics, 11 Science Park Road, Science Park II, 117685, Singapore

E-mail: eaqliu@ntu.edu.sg

Received 11 June 2004, in final form 6 September 2004

Published 25 October 2004

Online at stacks.iop.org/JMM/15/157

Abstract

Two novel lateral metal-contact radio-frequency microelectromechanical system (RF MEMS) switches are reported. These switches are implemented with quasi-finite ground coplanar waveguide (FGCPW) configuration and actuated by applying electrostatic force on a high-aspect-ratio cantilever beam. It is demonstrated that the insertion loss of the switch is less than 0.2 dB up to 15 GHz and the isolation is higher than 20 dB up to 25 GHz. An RF model of the switches is used to analyse the effects of the switch design parameters and RF performance. The optimization of the switch mechanical design is discussed where the threshold voltage can be lower than 25 V. The lateral switches are fabricated by deep reactive ion etching (DRIE) process on a silicon-on-insulator (SOI) wafer with shadow mask technology.

(Some figures in this article are in colour only in the electronic version)

1. Introduction

Microelectromechanical system (MEMS) switches have many potential applications including signal routing in transmit and receive applications, impedance matching networks, wide-band tuning networks, etc. In general, MEMS switches can be classified into two main categories based on the directions of motion, namely vertical switch and lateral switch. The vertical switch performs out of wafer plane displacement and surface contact. The lateral switch performs in wafer plane displacement and sidewall contact. Most of the reported MEMS switches are vertical motion switches, including the fixed–fixed beam switch [1], cantilever beam switch [2], toggle switch [3] and push–pull switch [4]. The main drawbacks of vertical switches are relatively complicated fabrication process and stiction problems during the release of the movable structures. Lateral motion switches have also been studied [5–12]. In contrast to vertical switches, lateral switches have the benefit of co-fabrication. The actuator, contacts, conductor paths and the support structures can be fabricated in a single lithographic step. Besides, it is easy to get a mechanical force in opposing directions even when electrostatic designs are used.

To date, lateral switches using three different fabrication processes have been reported. These include lateral switches

using nickel surface micromachining [5–7], thick polysilicon micromachining [8] and bulk micromachining [9, 10]. In the nickel surface micromachined switches [5–7], high-aspect-ratio structures are fabricated by electroplating nickel into lithographically defined plating stencils. The lithographic approach allows nickel heights of 10–50 μm with smallest widths of 5 μm . In the thick polysilicon micromachined switches [8], the mechanical structures were made using 2 μm polysilicon surface micromachining process with a sacrificial layer. In bulk micromachined switches [9, 10], the switches were fabricated using the DRIE process on an SOI wafer. The metal contact was realized by depositing a thin layer of metal directly on the whole surface of the switch structures. To avoid short circuits, the deposited metal has a thickness of less than 4000 \AA which limits the performance of the switch. None of these lateral switches exhibited acceptable RF performance at microwave frequencies due to the difficulties of integrating RF design and mechanical design. A study of a lateral switch with coplanar waveguide (CPW) configuration has been reported in earlier work [11, 12], which shows an insertion loss of below 1 dB and an isolation of above 16 dB in the frequency range of 400 MHz to 20 GHz.

In this paper, two different lateral metal-contact switches from 400 MHz to 25 GHz are investigated in detail. The FGCPW design based on SOI wafer will be introduced first in section 2. Then the design, modelling and simulation of two types of lateral metal-contact switches will be presented. In section 3, the mechanical design and optimization of the cantilever beam of switches are discussed, which provides analytical solution of the threshold voltage for the cantilever beam. The fabrication process using the DRIE process on an SOI wafer and shadow mask technology is then briefly presented in section 4. The fabricated switch shows low insertion loss and high isolation, which are comparable to the vertical switches. Finally, RF and mechanical measurement results of lateral switches are demonstrated and discussed in section 5. Conclusions are drawn in section 6.

2. RF design and simulation

2.1. Quasi-finite ground coplanar waveguide (FGCPW)

High resistivity (HR) silicon (Si) has been studied as a substrate material for communication system applications at microwave and millimetre wave frequencies for its mature fabrication process, low cost and acceptable RF performance [13]. By employing HR Si as a low-cost and low-loss substrate, relatively large area passive elements can be realized at millimetre wave frequencies [14]. In this paper, a quasi-FGCPW transmission line based on silicon-on-insulator (SOI) wafer is implemented for lateral switches. The cross-sectional view of the quasi-FGCPW transmission line is shown in figure 9(d). The transmission line consists of three parallel plate waveguides. Each waveguide is formed from a $35\ \mu\text{m}$ thick single-crystal-silicon plate that has been coated with a thin layer of aluminium (Al). Therefore, the RF signal can propagate not only along the metal on the top surface, but also along the metal on the sidewalls of the transmission line.

The FGCPW transmission line has been theoretically analysed using a three-dimensional (3D) full wave finite element method (FEM) analysis tool—Ansoft's high frequency structure simulator (HFSS). The material type and the resistivity of every layer of SOI were appropriately chosen in the simulation model to achieve a good match between the measured and the theoretical results. To accommodate $150\ \mu\text{m}$ pitch ground-signal-ground coplanar probes, the distance between the two ground lines, b , was chosen to be $200\ \mu\text{m}$ and the entire width of the FGCPW, c , was chosen to be between $400\ \mu\text{m}$ and $800\ \mu\text{m}$. The signal line width, a , was adjusted to be $66\ \mu\text{m}$ by HFSS to yield a characteristic impedance of about $50\ \Omega$. As shown in figure 1, the characteristic impedance of FGCPW is $50\ \Omega \pm 1\ \Omega$ up to 25 GHz.

2.2. Design of lateral switch and RF circuit

Two types of lateral switches are designed based on the quasi-FGCPW transmission line structure as shown in figures 2(a) and (b). The first type is a single-beam lateral switch which consists of an FGCPW transmission line and an electrostatic actuator. A cantilever beam is equipped with a fixed connection at one port. The free-end of the cantilever beam comes into contact with the contact tip at the other port upon turning on the switch. The cantilever beam serves as

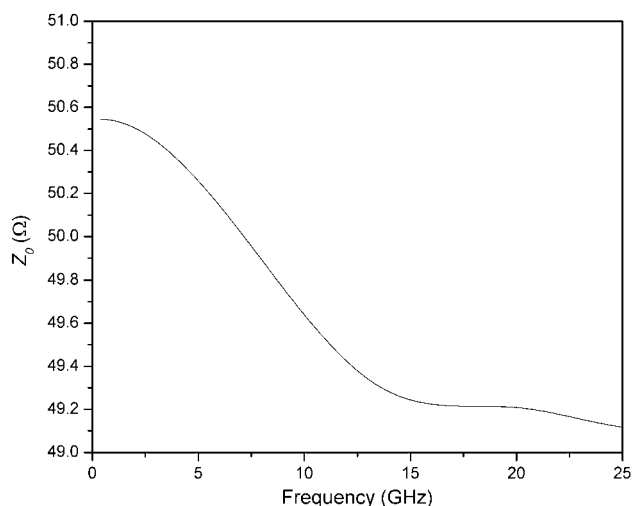
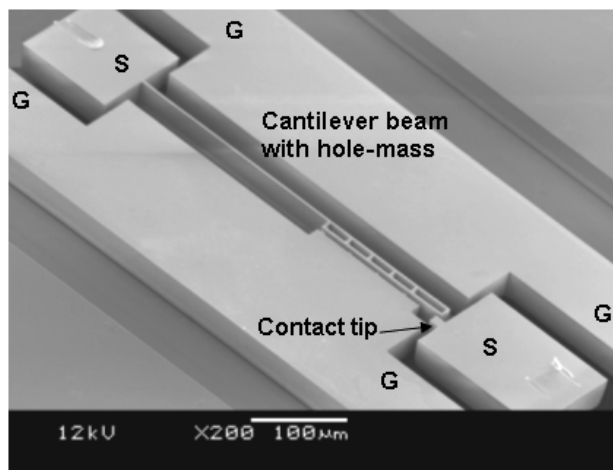
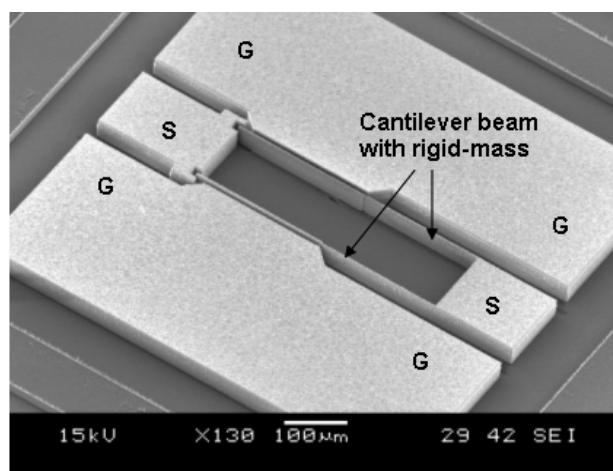


Figure 1. Characteristic impedance of an FGCPW with $0.5\ \mu\text{m}$ Al coating.



(a)



(b)

Figure 2. SEM micrographs of the two lateral switches: (a) single-beam switch and (b) double-beam switch (G: ground, S: signal).

a signal line and the ground lines beside the cantilever beam are extended towards the cantilever beam to avoid a drastic increase in the characteristic impedance. The width of the

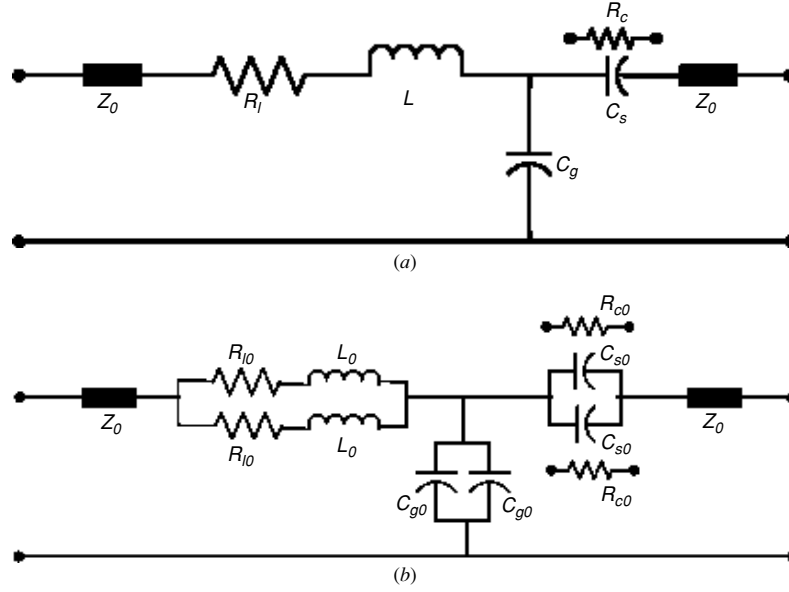


Figure 3. Equivalent circuit of lateral switches: (a) single-beam switch and (b) double-beam switch.

gaps between the cantilever beam and the ground lines, W' , is $30 \mu\text{m}$. The characteristic impedance of the cantilever beam section, Z_l , is about 78Ω simulated by HFSS. At the free-end of the cantilever beam, one ground line protrudes towards the cantilever beam further to serve as a fixed electrode. Therefore, no additional fixed electrode is required. When sufficient dc bias voltage is applied between the cantilever beam and the ground line, the cantilever beam is pulled towards the fixed electrode by the electrostatic force until its free-end touches the contact tip, resulting in the closed-state of the switch. Once the dc bias voltage is removed, the mechanical stresses in the beam overcome the stiction forces and pull the cantilever beam away, resulting in the open-state of the switch.

In the single-beam switch, only one cantilever beam is applied to serve as a movable electrode and signal line. In order to achieve low insertion loss and high power handling, double cantilever beams can be used as signal lines together to propagate RF signal. Based on the single-beam switch design, a newly designed double-beam switch is shown in figure 2(b). In this double-beam switch, two cantilever beams are employed. Both the fixed connections of the two cantilever beams are from the same port and the two contact tips are on the other port. At the free-end of the two cantilever beams, both ground lines extend towards the nearby cantilever beams to serve as their fixed electrodes respectively. Therefore, once sufficient dc bias voltage is applied between the signal line and two ground lines, both the cantilever beams will be pulled by the electrostatic force and move towards the two ground lines, respectively, until they touch the two contact tips on the same port.

2.3. RF modelling of the lateral switch

Figure 3(a) shows the equivalent circuit developed for the single-beam switch. The models consist of (1) characteristic impedance, Z_0 , of the input and output sections of the FGCPW transmission line, (2) the resistor, R_l , of a cantilever beam,

(3) the inductor, L , of a cantilever beam, (4) switch series capacitor, C_s (open-state), or contact resistor, R_c (closed-state), and (5) a shunt coupling capacitor, C_g . Figure 3(b) is the equivalent circuit developed for the double-beam switch, which can be reduced to the form of the equivalent circuit model of the single-beam switch. Therefore, for the double-beam switch, the whole beam resistor $R_l = R_{l0}/2$, inductor $L = L_0/2$, series capacitor of open switch $C_s = 2C_{s0}$, contact resistor of closed switch $R_c = R_{c0}/2$ and shunt capacitance $C_g = 2C_{g0}$, assuming that the two cantilever beams are identical. Hence, only the circuit model of the single-beam switch is discussed in this section, which could also be used for the double-beam switch model. The circuits were modelled using Agilent EESof's Advanced Design System (ADS). The cantilever beam resistance R_l , inductance L , switch open capacitance C_s and closed resistance R_c and shunt capacitance C_g are allowed to vary to fit the model in the simulated or measured S -parameters using ADS.

Based on the T -equivalent circuit model, S_{21} of the whole circuit of the single-beam switch can be given by [15]

$$S_{21} = \frac{2}{2 + (Z_0 + Z_1 + Z_2)/Z_3 + (Z_1 + Z_2 + \frac{Z_1 Z_2}{Z_3})/Z_0} \quad (1)$$

where

$$Z_1 = R_l + j\omega L \quad (2a)$$

$$Z_2 = \begin{cases} \frac{1}{j\omega C_s} & \text{at the open state} \\ R_c & \text{at the closed state} \end{cases} \quad (2b)$$

$$Z_3 = \frac{1}{j\omega C_g} \quad (2c)$$

with ω the angular frequency ($\omega = 2\pi f$, f is the signal frequency).

In the open state, the switch performance is determined by the switch capacitance C_s . For $S_{21} \ll -10 \text{ dB}$ and

$\omega C_s Z_0 [2 - \omega^2 C_g L + \frac{C_g}{C_s} + \frac{R_l}{Z_0} (1 + \frac{C_g}{C_s})] \ll 1$, the switch isolation can be approximately expressed as

$$S_{21} \approx 2j\omega C_s Z_0. \quad (3)$$

Therefore, the series capacitance of the open-state of the switch, C_s , can be extracted from the measured isolation of the switch using equation (3). The isolation of the open switch increases with the decrease in C_s . The equivalent series capacitance C_s of the lateral switch is approximately 4–10 fF and the isolation is higher than 20 dB up to 25 GHz.

At low frequencies, $\omega [C_g (Z_0 + R_l + R_c + R_l R_c / Z_0) + L / Z_0] \ll 2 + (R_l + R_c) / Z_0$ and $\omega^2 C_g L (1 + R_c / Z_0) \ll 2 + (R_l + R_c) / Z_0$, the insertion loss and return loss of the switch can be simplified as

$$S_{21} \approx 2 / [2 + (R_l + R_c) / Z_0] \quad (4a)$$

$$S_{11} \approx (R_l + R_c) / [2Z_0 + (R_l + R_c)]. \quad (4b)$$

The RF performances of the closed-state of the switch deteriorate with the increase in the total resistance ($R_l + R_c$). When $R_l + R_c < 2 \Omega$, the insertion loss is less than 0.2 dB up to 10 GHz. However, when ($R_l + R_c$) increases to 10 Ω the insertion loss is larger than 0.8 dB at 10 GHz. The total resistance ($R_l + R_c$) of the closed-state of the switch can also be extracted from the measured insertion loss of the switch using equation (4). Therefore, the total resistance ($R_l + R_c$) should be less than 2 Ω . It is found that the measured total resistance ($R_l + R_c$) decreases with the increase in the thickness of the deposited Al since the cantilever beam resistance R_l is determined by the thickness of the deposited Al. The skin depth of Al is 0.85 μm at 10 GHz and 0.54 μm at 25 GHz. For thin Al deposition ($t < 1 \mu\text{m}$), the beam resistance is constant up to 25 GHz and can be expressed as

$$R_l = \rho \sum_i \frac{l_i}{A_i} \quad (5)$$

where ρ is the resistivity of Al ($\rho = 2.85 \times 10^{-8} \Omega \text{m}$), l_i is the length of the different sections of the cantilever beam, A_i is the total cross-sectional area of Al wrapped around the single crystal silicon at different sections of the cantilever beam.

The series inductance L can be calculated by [15]

$$L = \frac{Z_l \beta l}{\omega} = \frac{Z_l l \sqrt{\epsilon_{\text{eff}}}}{c} \quad (6)$$

where Z_l is the impedance of the cantilever beam, l is the whole length of the cantilever beam, β is the phase constant, ϵ_{eff} is the relative effective permittivity and c is the speed of light in a vacuum ($c = 3.0 \times 10^8 \text{ m s}^{-1}$). According to the current design parameters, $l = 400\text{--}500 \mu\text{m}$, $Z_l = 50\text{--}78 \Omega$, $\epsilon_{\text{eff}} \approx 1.66$, the equivalent series inductance is 86–167 pH. The simulation results of the closed-state of the switch are better as inductance increases from 10 pH to 100 pH as shown in figure 4. However, when the inductance L is increased further, the insertion loss and return loss begin to deteriorate.

The shunt coupling capacitance, C_g , between the cantilever beam and the fixed electrode can be estimated as

$$C_g = \frac{\epsilon_0 l_2 h}{g_0 - y} + C_f \quad (7)$$

where ϵ_0 is the permittivity of the air ($8.854 \times 10^{-12} \text{ F m}^{-1}$), l_2 is the length of the electrode part of the cantilever beam, h is

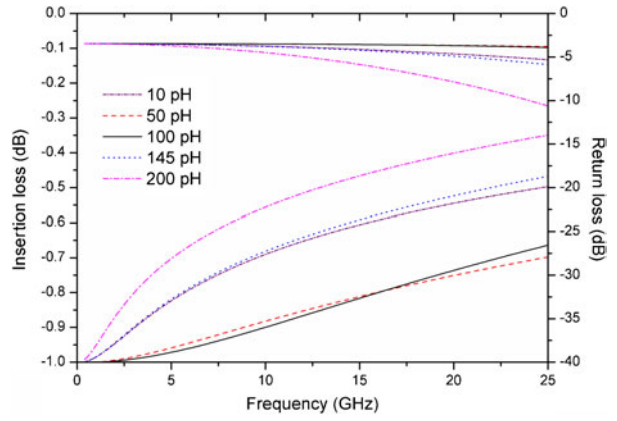


Figure 4. Simulated S -parameters of a switch in the closed-state with various inductances L .

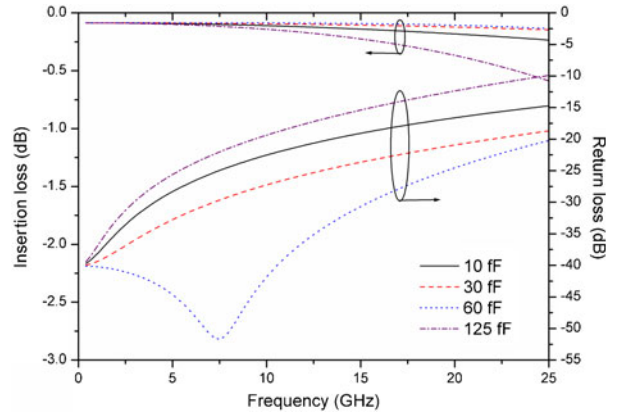


Figure 5. Simulated S -parameters of a switch in the closed-state with various capacitances C_g .

the height of the cantilever beam, g_0 is the original gap distance between two electrodes, y is the displacement of the electrode part of the cantilever beam, C_f is the fringing field capacitance which is about 60% of C_g . This coupling capacitance is fairly large ($C_g \gg C_s$) and affects the loss mechanism in the closed-state of the switch. Figure 5 shows the ADS simulation results of the effect of C_g on the S -parameters of the switch at the closed-state. The insertion loss and the return loss of the closed-state of the switch improve when C_g increases from 10 fF to 60 fF. The performance of the closed-state of the switch begins to deteriorate when C_g is increased further to 125 fF. Therefore, in order to design a high performance RF lateral switch with high return loss, low insertion loss and low threshold voltage, the design parameters l_2 and g_0 have to be carefully selected and optimized.

3. Mechanical design and simulation

The fundamental design of the lateral switch is based on an electrostatic actuator with a typical plan-view schematic shown in figure 6. The actuator consists of four components: (1) a 35 μm deep suspended cantilever beam serving as a movable electrode, (2) an anchor on the substrate supporting the cantilever beam, (3) a fixed electrode on the opposite side of the cantilever beam, and (4) a contact tip on the substrate.

The cantilever beam OC is a beam-mass structure. For the beam part OA, the width is w_1 and the length is l_1 . For the

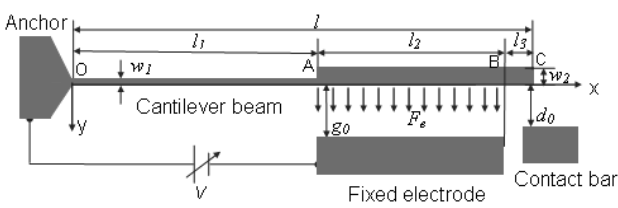


Figure 6. Plan-view schematic of an electrostatic actuator.

mass part AC, the width is w_2 and the length is $(l_2 + l_3)$ in which l_2 is the length of the electrode section AB and l_3 is the length of BC. The mass width w_2 is designed to be relatively wider than the beam width w_1 so that low threshold voltage can be maintained and large deformation of the electrode section can be avoided. Hence, no separate bumpers or landing pads are required to avoid short circuit between the two electrodes as other lateral switches [11] did.

The original distance between the two electrodes is g_0 and between the mass and the contact tip is d_0 . g_0 is relatively bigger than d_0 so that the cantilever beam will touch the contact tip first once the switch is actuated. In the model, X and Z axes are assumed to be oriented parallel to the length and depth of the cantilever beam respectively, and the Y-axis is directed towards the fixed electrode.

3.1. Electrostatic force F_e

When a dc bias voltage, V , is applied between the two electrodes, the electrostatic force causes the mass to move towards the fixed electrode and the beam is bent. The bending of the mass is negligible because it has much higher flexure rigidity than the beam. The displacement of the mass increases with voltage until pull-in occurs. Assuming that the displacement of the part of the beam OA and mass AC are $y_1(x)$ and $y_2(x)$ respectively, the electrostatic force F_e on the mass can be given as

$$F_e = \int_{l_1}^{l_1+l_2} \frac{\epsilon_0 h V^2 dx}{2(g_0 - y_2)^2} = \frac{\epsilon_0 h l_2 V^2}{2(g_0 - \alpha - \theta l_2)(g_0 - \alpha)} \quad (8)$$

where

$$y_2(x) = \alpha + \theta(x - l_1), \quad l_1 \leq x \leq l_1 + l_2 \quad (9)$$

with α the displacement of point A and θ the angle of point A. When $\theta l_2 \ll \alpha$, as a first-order approximation, equation (8) can be simplified as

$$F_e = \frac{\epsilon_0 h l_2 V^2}{2(g_0 - \alpha)^2}. \quad (10)$$

3.2. Restoring force F_r and equivalent stiffness k

Once the mass is displaced, an elastic restoring force by the beam tends to pull the mass back towards its original position. At the end of the electrode part AB of the mass, the restoring force F_r can be written as

$$F_r = -k y_2(l_1 + l_2) = -k(\alpha + \theta l_2) \quad (11a)$$

where k is the equivalent stiffness of the cantilever beam. When $\theta l_2 \ll \alpha$, F_r can be approximately given by

$$F_r = -k\alpha. \quad (11b)$$

Supposing that the mass is subject to a concentrated force at the midpoint of the mass based on the method of superposition [16], the equivalent stiffness k can be derived as

$$k = \frac{12E_1 I_1 E_2 I_2}{E_2 I_2 (4l_1^3 + 9l_1^2 l_2 + 6l_1 l_2^2) + 5E_1 I_1 l_2^3 / 4} \quad (12)$$

where E_2 is Young's modulus of the mass and I_2 is the moment of inertia of the cross-sectional area of the mass. Before the deposition of the metal, the beam is merely made up of single crystal silicon. E_1 , E_2 , I_1 and I_2 are given by

$$E_1 = E_2 = E_{Si} \quad (13a)$$

$$I_1 = \frac{1}{12} w_1^3 h \quad (13b)$$

$$I_2 = \frac{1}{12} w_2^3 h \quad (13c)$$

where E_{Si} is Young's modulus of the single crystal silicon ($E_{Si} \approx 140$ GPa). After the deposition of Al, the beam is made of single crystal silicon wrapped around by Al. Therefore, E_1 , E_2 , I_1 and I_2 can be expressed as

$$E_1 = \frac{E_{Si} w_1 + 2E_{Al} w_{Al}}{w_1 + 2w_{Al}} \quad (14a)$$

$$E_2 = \frac{E_{Si} w_2 + 2E_{Al} w_{Al}}{w_2 + 2w_{Al}} \quad (14b)$$

$$I_1 = \frac{1}{12} (w_1 + 2w_{Al})^3 h \quad (14c)$$

$$I_2 = \frac{1}{12} (w_2 + 2w_{Al})^3 h \quad (14d)$$

where E_{Al} is Young's modulus of Al ($E_{Al} = 70$ GPa), w_{Al} is the thickness of Al deposited at the sidewalls of the silicon beam. Since $E_{Si} w_1 \approx 10E_{Al} w_{Al}$, the equivalent stiffness of the whole structure is dominated by the silicon structures.

3.3. Threshold voltage V_{th}

Based on the balanced position of the mass, the relation of forces can be found as

$$F = F_e + F_r = 0. \quad (15)$$

When the applied bias voltage V is equal to a specific voltage—threshold voltage V_{th} , equation (15) has only one solution. At this point, the mass position becomes unstable due to the positive feedback in the electrostatic actuation. When $V < V_{th}$, equation (15) has two solutions, i.e. the mass has two possible beam positions for every applied voltage. When $V > V_{th}$, equation (15) does not have solutions since $F_e > -F_r$ at all displacements, i.e. the mass will always collapse to touch the contact tip. As a first-order approximation, when $\alpha = \frac{1}{3}g_0$, the threshold voltage V_{th} can be found to be

$$V_{th} = \sqrt{\frac{8kg_0}{27\epsilon_0 l_2 h}}. \quad (16)$$

Figure 7 shows the simulation results of the shape of a cantilever beam ($l_1 = 275 \mu\text{m}$, $l_2 = 165 \mu\text{m}$, $l_3 = 10 \mu\text{m}$, $w_1 = 2.5 \mu\text{m}$, $w_2 = 5 \mu\text{m}$, $w_{Al} = 0.6 \mu\text{m}$, $g_0 = 4.8 \mu\text{m}$, $d_0 = 2.8 \mu\text{m}$) with various bias voltages, which is simulated using commercial software—LS DYNA. The displacement of the cantilever beam increases with the increase in applied bias voltage. From figure 7 the simulated threshold voltage

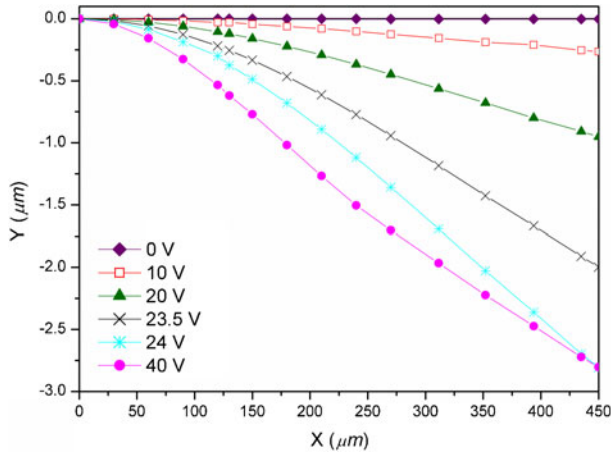


Figure 7. The shape of the cantilever beam with various applied bias voltages.

is 24 V and is very close to the value calculated using equation (16). The deformation of the beam OA of the cantilever beam increases with the bias voltage, whereas the mass AC of the cantilever beam moves almost without deformation.

Based on equation (16), the threshold voltage V_{th} is determined by the cantilever beam design and the original gap between the two electrodes g_0 . Figure 8 shows that the threshold voltage V_{th} decreases as the original gap between the two electrodes g_0 decreases or the length sum $(l_1 + l_2)$ increases. When the cantilever beam length ratio $l_2/(l_1 + l_2)$ is in the range of 35–75%, V_{th} only change within 10% of the minimum V_{th} , which is referred to as $\text{MIN}[V_{th}]$. The corresponding length

ratio $\text{MIN}[l_2/(l_1 + l_2)]$ to $\text{MIN}[V_{th}]$ is 57% when $w_1 = 2.5 \mu\text{m}$, $w_2 = 5 \mu\text{m}$ and $w_{Al} = 0$. It also shows that $\text{MIN}[l_2/(l_1 + l_2)]$ is independent of the initial gap g_0 and length sum $(l_1 + l_2)$.

The effect of the beam parameters w_1 , w_2 and w_{Al} on the threshold voltage V_{th} is summarized in table 1. It shows that V_{th} is more dependent on the beam width w_1 than on the mass width w_2 and Al thickness on sidewalls w_{Al} . The effect of the mass width w_2 is negligible when $w_1 \leq w_2$. V_{th} increases with the increase in w_1 . The effect of w_{Al} on V_{th} is more complicated. Initially when w_{Al} increases, V_{th} increases a little. However, after V_{th} gets to its maximum value, it decreases with the increase in w_{Al} . This observation can be explained by the two effects that arise from the metal deposition on the sidewalls. On the one hand, it increases the stiffness of the cantilever beam which tends to increase the restoring force F_r and the threshold voltage V_{th} . On the other hand, it reduces the original gap between the two electrodes from g_0 to $(g_0 - 2w_{Al})$ which tends to increase the electrostatic force F_e and reduce V_{th} . When w_{Al} is small, the increase in F_r dominates the increase in F_e . As a result V_{th} increases. However, once w_{Al} exceeds a specific value, the increase in F_e dominates the increase in F_r . Therefore V_{th} falls. Generally, the change of V_{th} due to the metal deposition on the sidewalls is less than 5 V since w_{Al} is less than $1 \mu\text{m}$.

4. Fabrication process

The lateral switches were fabricated on an SOI wafer, which includes a $35 \mu\text{m}$ thick low resistivity (LR) device active silicon (Si) layer ($<0.1 \Omega \text{cm}$), a $2 \mu\text{m}$ thick buried thermal silicon dioxide (SiO_2) layer and a $500 \mu\text{m}$ thick high

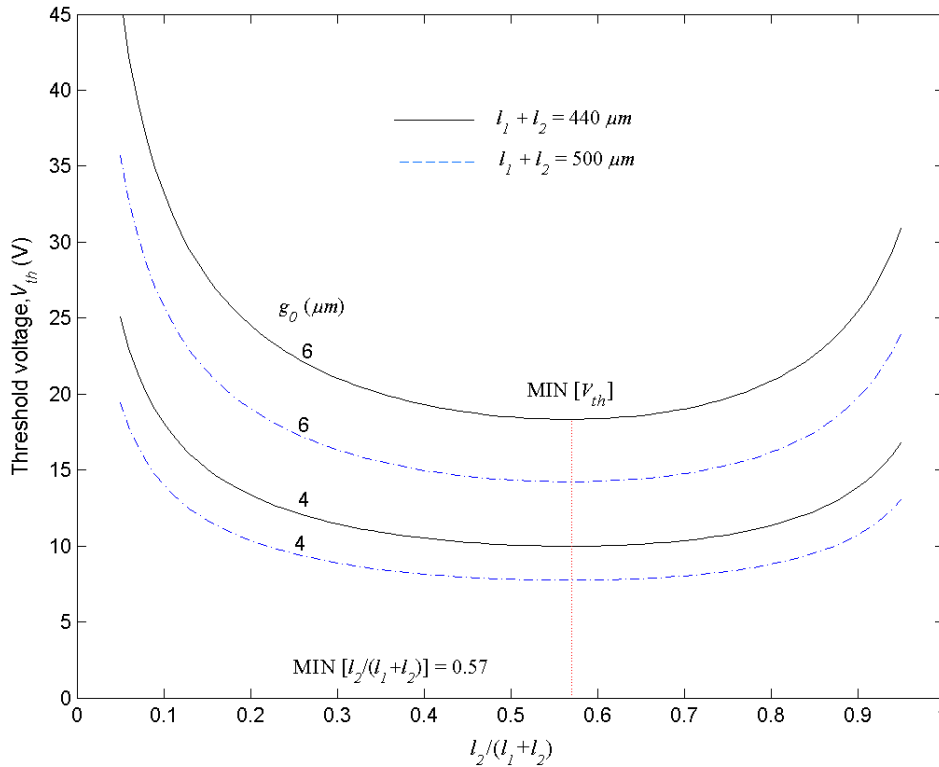


Figure 8. Calculated threshold voltage V_{th} with various lengths $(l_1 + l_2)$, $l_2/(l_1 + l_2)$ ratio and initial gap distance g_0 ($w_1 = 2.5 \mu\text{m}$, $w_2 = 5 \mu\text{m}$, $w_{Al} = 0$).

Table 1. The effect of the cantilever beam design parameters on the threshold voltage.

Beam width w_1 (μm)	Mass width w_2 (μm) ($w_{\text{Al}} = 0$)			Al thickness at sidewalls w_{Al} (μm) ($w_2 = 5 \mu\text{m}$)		
	2.5	5	15	0.2	0.6	1.0
2.0	13.97	14.062	14.075	15.953	18.339	18.722
2.5	19.387	19.634	19.669	21.335	23.13	22.724
3.0	25.225	25.776	25.854	27.193	28.253	26.953
3.5	31.344	32.421	32.578	33.479	33.679	31.391

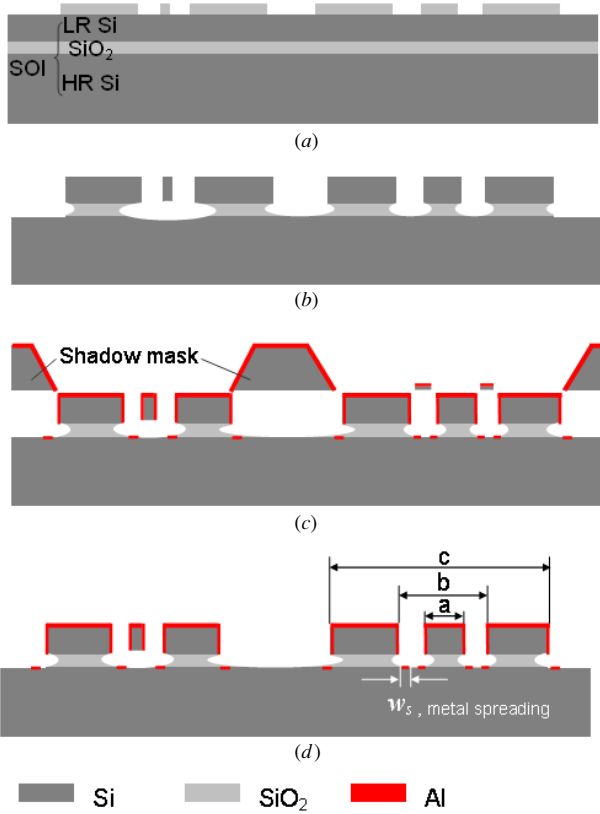


Figure 9. Fabrication process flow. (a) SiO_2 deposition and patterning on the surface of LR Si. (b) LR Si trench-etched by DRIE. SiO_2 was etched using BOE. (c) Al coating through a shadow mask. (d) Shadow mask de-bonded.

resistivity (HR) handle silicon layer ($>4000 \Omega \text{ cm}^{-1}$). The fabrication process flow is shown in figure 9.

The process began with the deposition of $2.0 \mu\text{m}$ thick SiO_2 on an SOI substrate using plasma-enhanced chemical vapour deposition (PECVD) and patterning using reactive ion etching (RIE), as seen in figure 9(a). Then, DRIE was employed to etch the LR Si into the buried SiO_2 layer using the top SiO_2 as the hard mask. The movable cantilever beam was released by removing the sacrificial material-buried thermal SiO_2 using buffered oxide etchant (BOE). At the same time, the exposed top SiO_2 was removed (figure 9(b)). Following this step, the SOI wafer was temporarily bonded to a shadow mask [17] using photoresist as intermediate material. A 0.8 – $1.5 \mu\text{m}$ thick Al film was deposited on both the surface and the sidewalls of the switches through the shadow mask via evaporation (figure 9(c)). Finally, the shadow mask was de-

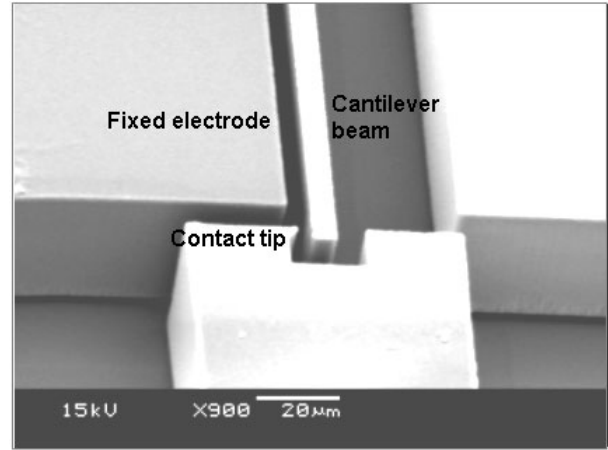


Figure 10. SEM micrograph of the contact part of the lateral switches.

bonded by heating the two wafers at $150 \text{ }^\circ\text{C}$ and manually separated from the SOI substrate when the photoresist turned soft. The photoresist that remained on the SOI wafer was wiped up using acetone (figure 9(d)).

The yield of this process is very high ($>90\%$) due to the high-aspect-ratio single-crystal-silicon structures which are free from warping, pre-deformation and sticking during the wet etching process. Due to the nature of the evaporation process, the Al coated on the sidewalls is thinner than that coated on the surface. It is observed that the metal deposited on the surface is $1.5 \mu\text{m}$ thick and the metal deposited on the sidewall is about $0.63 \mu\text{m}$ thick when $1.5 \mu\text{m}$ thick Al is evaporated through a shadow mask.

Figure 2 shows the SEM micrographs of the two types of lateral switches. The sizes of the fabricated single-beam switch and double-beam switch are $400 \mu\text{m} \times 700 \mu\text{m}$ and $800 \mu\text{m} \times 700 \mu\text{m}$ in area, respectively. A hole-mass structure is employed in the cantilever beam of the single-beam switch, as shown in figure 2(a). Compared to the rigid mass, the hole mass has three advantages. Firstly, a rigid mass which is wider than $5 \mu\text{m}$ cannot be released due to the constriction in the fabrication process. However, this problem can be solved by the mass with etched holes. Secondly, the etched holes reduce the effective mass of the mass structure. Thirdly, the lateral switch with hole-mass structure can provide better RF performance than that with rigid-mass structure, which will be discussed in section 5.1. Besides, as discussed in section 3.3, the hole mass will not increase the threshold voltage of the switch. The enlarged view of the contact bar of a lateral switch is shown in figure 10, in which the contact tip is a triangular tip.

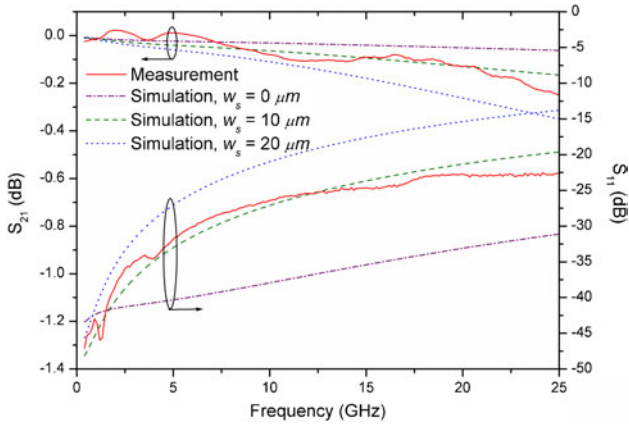


Figure 11. Comparison of measured and simulated results of FGCPW with 1.5 μm thick Al deposition.

5. Experimental results and discussions

5.1. RF measurements

The RF responses of the FGCPW and lateral switches were measured using the HP 8510C Vector Network Analyzer with tungsten-tip 150 μm pitch Cascade Microtech ground-signal-ground coplanar probes. The system was calibrated using standard short-open-load-through (SOLT) on-wafer calibration technique. All tests were performed in the room environment without any packaging.

The measured and simulated S -parameters of a 1 mm long FGCPW with 1.5 μm Al deposition are shown in figure 11. The insertion loss and return loss of FGCPW are 0.13 dB and 22 dB at 20 GHz respectively. However, it is found that the measured performance of FGCPW is inferior compared to the simulated results ($w_s = 0$). This can be explained by some metal spread on the handle layer through the shadow mask, as shown in figure 9(d), which increases the coupling loss between the FGCPW transmission line and the substrate. The thicker the metal deposit, the more serious the metal spreading effect. Figure 11 indicates an Al spread about 10 μm wide on the handle layer when 1.5 μm thick Al was deposited.

Figure 12 shows the comparison of the measured S -parameters of the two types of lateral switches with 1.2 μm thick Al deposition. Up to 25 GHz, both lateral switches have an insertion loss of less than 1 dB, return loss and isolation of higher than 17 dB. The insertion loss of the double-beam switch is lower than that of the single-beam switch by 0.1 dB. The return loss and isolation of both switches are very close. In general, the design of the double-beam lateral switch provides a perfect RF symmetrical circuit, where the advantages of the double-beam lateral switch are lower insertion loss and higher power handling compared with the single-beam lateral switch. However, there is a potential problem of the characteristic impedance change of the transmission line, when the two cantilever beams are mismatched between the two paths. The RF experimental results and fitted circuit parameters of the two different designs of the lateral switch at 10 GHz are listed in table 2.

The cantilever beam serves as the main part of the signal line in the lateral switches where the design parameters (beam width, mass shape and length) of the cantilever beam are

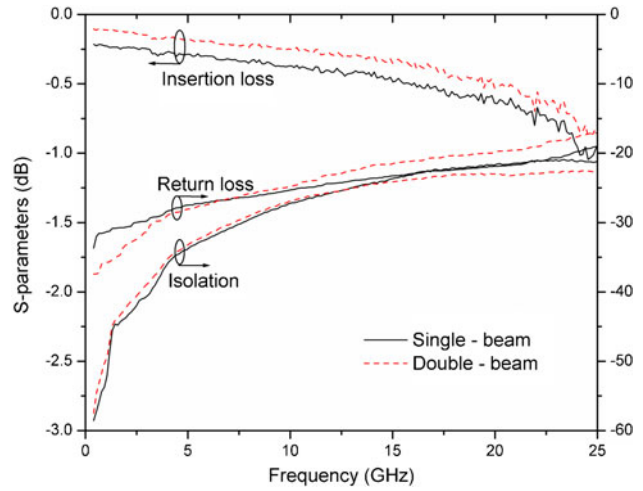


Figure 12. Comparison of measured S -parameters of the two lateral switches ($l_1 = 275 \mu\text{m}$, $l_2 = 165 \mu\text{m}$, $l_3 = 10 \mu\text{m}$, $w_1 = 2.5 \mu\text{m}$, $w_2 = 5 \mu\text{m}$, $g_0 = 6 \mu\text{m}$, $d_0 = 4 \mu\text{m}$).

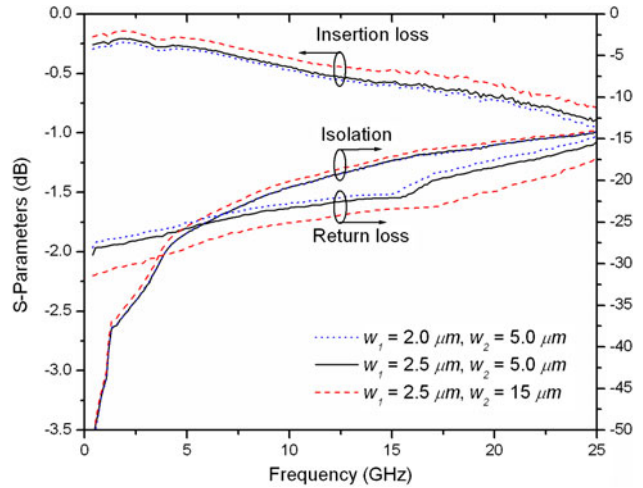


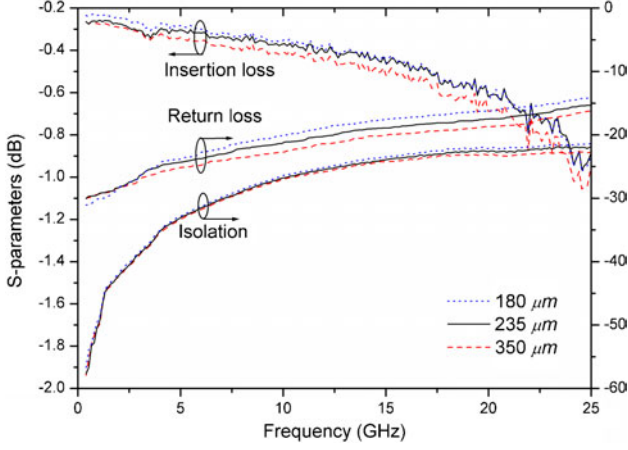
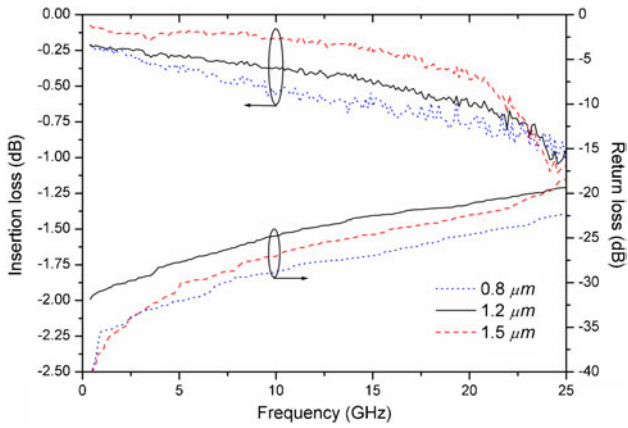
Figure 13. Comparison of S -parameters of the single-beam switch with various w_1 , w_2 and w_{Al} ($l_1 = 210 \mu\text{m}$, $l_2 = 215 \mu\text{m}$, $l_3 = 21.5 \mu\text{m}$, $g_0 = 6 \mu\text{m}$ and $d_0 = 4 \mu\text{m}$).

important in determining the RF performance of the lateral switches. Figure 13 shows the comparison of measured S -parameters of a single-beam switch with different beam width w_1 and mass width w_2 . Al deposited is 1.2 μm thick. It is found that the switch with w_1 of 2.5 μm has lower insertion loss and higher return loss than that with w_1 of 2 μm . This is because the latter has higher beam resistance and inductance than the former. The isolations of both switches are almost the same. The insertion loss and return loss of the switch with hole mass ($w_2 = 15 \mu\text{m}$) are slightly better than those of the switch with rigid mass ($w_2 = 5 \mu\text{m}$). The isolation of the switch with rigid mass is higher than that of the switch with hole mass by about 1 dB. This is because the hole mass offers lower series resistance R_l and inductance L than the rigid mass.

When $(l_1 + l_2)$ and l_3 are kept constant, changing the length of the electrode part of the mass, l_2 can affect the RF performance of the lateral switch due to the shunt coupling capacitance C_g effect. Figure 14 shows the comparison of measured S -parameters of a double-beam switch with various electrode lengths l_2 when $(l_1 + l_2)$ and l_3 are kept at 425 μm

Table 2. The RF experimental results and fitted circuit parameters of the two different designs of the lateral switch at 10 GHz.

	Insertion loss (dB)	Return loss (dB)	Isolation (dB)	R_l (Ω)	L (pH)	C_g (fF)	C_s (fF)	R_c (Ω)
Single-beam switch	0.37	25.3	27.2	0.4	148	28	6.7	2.2
Double-beam switch	0.25	24.8	26.8	0.2	70	60	6.9	0.9


Figure 14. Comparison of S -parameters of the double-beam switch with various electrode lengths l_2 ($l_1 + l_2 = 425 \mu\text{m}$).

Figure 15. Comparison of S -parameters of the single-beam switch with various thicknesses of Al deposition in the closed-state ($l_1 = 275 \mu\text{m}$, $l_2 = 165 \mu\text{m}$, $l_3 = 10 \mu\text{m}$, $w_1 = 2.5 \mu\text{m}$, $w_2 = 5 \mu\text{m}$, $g_0 = 6 \mu\text{m}$ and $d_0 = 4 \mu\text{m}$).

and $25 \mu\text{m}$ respectively. The other elements of the switch design parameters are $w_1 = 2.5 \mu\text{m}$, $w_2 = 5 \mu\text{m}$, $g_0 = 6 \mu\text{m}$, $d_0 = 4 \mu\text{m}$, and $1.2 \mu\text{m}$ thick Al deposition. The insertion loss increases from 0.35 dB to 0.41 dB at 10 GHz when l_2 increases from $180 \mu\text{m}$ to $350 \mu\text{m}$, whereas the return loss increases from 20.6 dB to 23.6 dB . The isolations of the switches change marginally.

Due to the skin effect of metal in the high frequency range, the thickness of metal deposition affects the RF performance of the closed-state of the switches. Figure 15 shows the comparison of measured S -parameters of a single-beam switch with various thicknesses of Al deposition of the switches. The insertion loss of the switch decreases from 0.62 dB to 0.2 dB at 15 GHz when the Al thickness increases from $0.8 \mu\text{m}$ to $1.5 \mu\text{m}$. The return loss is higher than 20 dB up to 25 GHz .

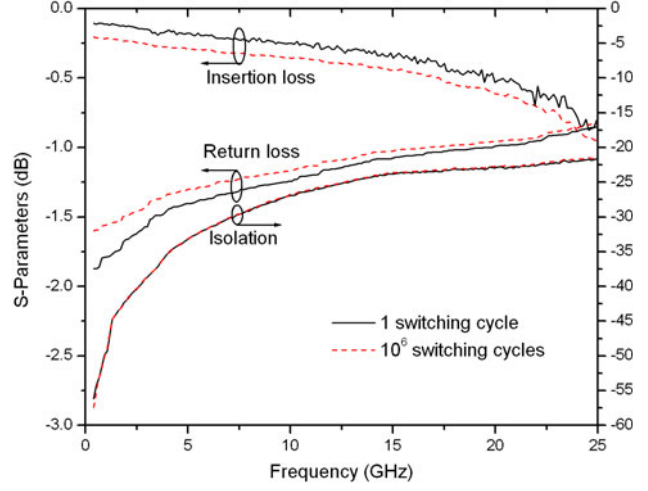
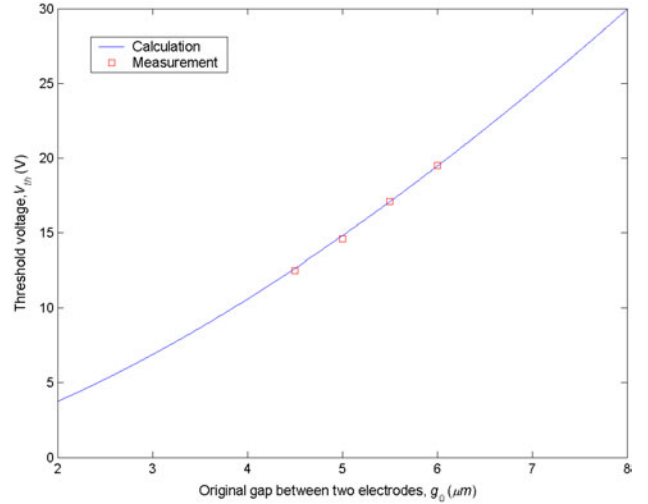

Figure 16. Effect of switching cycles on the S -parameters of the double-beam switch.

Figure 17. Measured and calculated threshold voltage V_{th} of the lateral switch with various g_0 ($l_1 = 220 \mu\text{m}$, $l_2 = 210 \mu\text{m}$, $l_3 = 10 \mu\text{m}$, $w_1 = 2.5 \mu\text{m}$, $w_2 = 5 \mu\text{m}$, $w_{Al} = 0 \mu\text{m}$).

Figure 16 shows that the insertion loss and the return loss of the double-beam switch deteriorate by 0.1 dB and 1.5 dB at 10 GHz , respectively, after one million cold switching cycles. The high-aspect-ratio deep etch fabrication technique does not only provide highly reliable switches, but the thickness of the Al deposition through the shadow mask technology also provides low insertion loss and high isolation switch.

5.2. Mechanical measurements

Since the pull-in of the cantilever beam is sharp and sudden, accurate measurement of the threshold voltage required for reaching pull-in can be easily performed at wafer level using the standard electrical test equipment with a microscope.

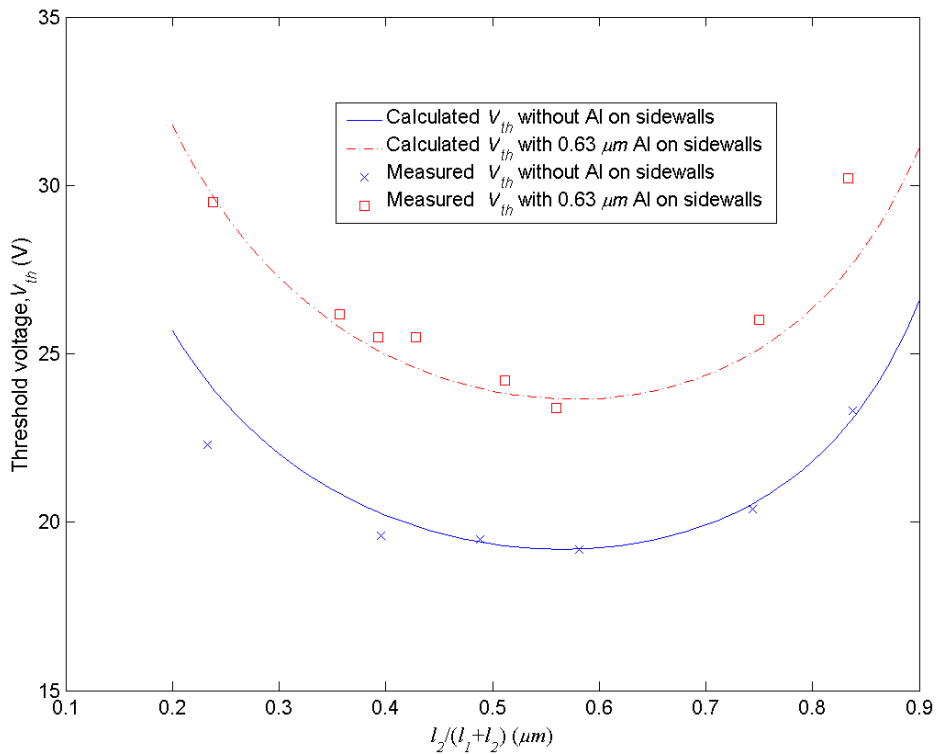


Figure 18. Measured and calculated threshold voltage V_{th} with various $(l_2/(l_1 + l_2))$ ratios before and after Al deposition ($l_1 + l_2 = 430 \mu\text{m}$, $l_3 = 10 \mu\text{m}$, $w_1 = 2.5 \mu\text{m}$, $w_2 = 5 \mu\text{m}$, $g_0 = 6 \mu\text{m}$).

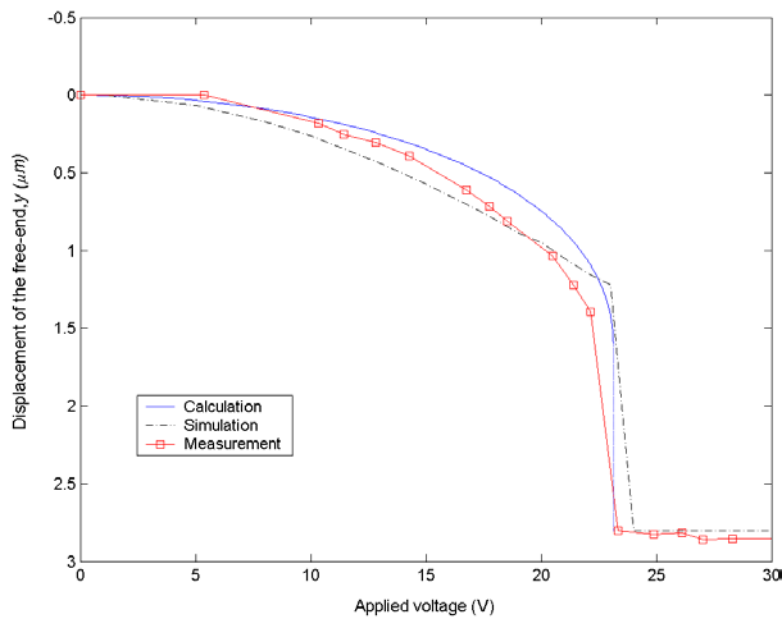


Figure 19. Comparison of measured, calculated and simulated displacement of the free-end of the cantilever beam with $0.63 \mu\text{m}$ thick Al on sidewalls ($l_1 = 275 \mu\text{m}$, $l_2 = 165 \mu\text{m}$, $l_3 = 10 \mu\text{m}$, $w_1 = 2.5 \mu\text{m}$, $w_2 = 5 \mu\text{m}$, $w_{Al} = 0.63 \mu\text{m}$).

Figure 17 shows the comparison of the measured and calculated threshold voltages V_{th} of the lateral switch with various original gap distances g_0 , where $l_1 = 220 \mu\text{m}$, $l_2 = 210 \mu\text{m}$, $l_3 = 10 \mu\text{m}$, $w_1 = 2.5 \mu\text{m}$, $w_2 = 5 \mu\text{m}$ and $w_{Al} = 0 \mu\text{m}$. The threshold voltage V_{th} increases with the increase in g_0 . An increase in g_0 by $0.5 \mu\text{m}$ increased the threshold voltage V_{th} by about 2.5 V . The effect of the $(l_2/(l_1 + l_2))$ ratio on the threshold voltage V_{th} is shown in figure 18. The threshold voltage V_{th} is $20 \pm 1 \text{ V}$ when

the $(l_2/(l_1 + l_2))$ ratio is in the range of 35–75% before the metal deposition. Figure 18 also shows the metal deposition effect on the threshold voltage. When $0.63 \mu\text{m}$ thick Al is deposited on the sidewalls of lateral switches, the threshold voltage of the switch increases by approximately 5 V .

Figure 19 shows the comparison between the measured, calculated and simulated displacement results of the free-end of a lateral switch with $0.63 \mu\text{m}$ thick Al on sidewalls. The displacement of the free-end of the cantilever beam increases

with the increase in the applied dc bias voltage. When the bias voltage increases to 23.3 V, the cantilever beam is attracted to touch the contact tip rapidly from 1.4 μm away. Therefore, the threshold voltage of this switch is 23.3 V. The measurement result shows a close agreement with the calculated result and the simulated result.

6. Conclusions

In this paper, two different lateral switches, a single-beam switch and a double-beam switch for up to 25 GHz applications are designed, simulated and fabricated where the lateral switches are implemented with a quasi-FGCPW and an electrostatic actuator. The measurement results show that the lateral switches have low insertion loss (<1 dB) and high isolation (>20 dB) up to 25 GHz. However, the insertion loss of the double-beam switch is lower than that of the single-beam switch by 0.1 dB, though there are slight variations in return loss and isolation. A high-aspect-ratio cantilever beam with beam-mass structure is employed as the actuation part of the lateral switches, which provides low threshold voltage of less than 25 V and high reliability of more than one million cold switching cycles. The DRIE fabrication process on an SOI wafer was utilized to fabricate the lateral switches and a shadow mask was used to deposit metal on the sidewall of the switches. The lateral switches have broad potential applications in the high frequency transmitting/receiving circuit, true-time-delay phase shifter and switching matrix.

Acknowledgments

The authors are especially grateful to Associate Professor Law Choi Look for his help and support. We would like to express our appreciation to all technicians at Wireless Technology and Position Center (WTPC) and Photonics Research Center (PhRC) for their technical support for the RF MEMS device characterization and measurement.

References

- [1] Goldsmith C L, Yao Z, Eshelman S and Denniston D 1998 Performance of low-loss RF MEMS capacitive switches *IEEE Microw. Guid. Wave Lett.* **8** 269–71

- [2] Hyman D *et al* 1999 GaAs compatible surface-micromachined RF MEMS switches *Electron. Lett.* **35** 224–5
- [3] Schauwecker B, Strohm K A, Simon W, Mehner J and Luy J-F 2002 Toggle-switch—a new type of RF MEMS switch for power applications *IEEE MTT-S Int. Microwave Symp. Digest* pp 219–22
- [4] Hah D, Yoon E and Hong S 2000 A low-voltage actuated micromachined microwave switch using torsion springs and leverage *IEEE Trans. Microw. Theory Tech.* **48** 2540–6
- [5] Wood R, Mahadevan R, Dhuler V, Dudley B, Cowen A, Hill E and Markus K 1998 MEMS microrelay *Mechatronics* **8** 535–47
- [6] Roy S and Mehregany M 1995 Fabrication of electrostatic nickel microrelays by nickel surface micromachining *IEEE MEMS'95 Proc.* pp 353–7
- [7] Roth S, Marxer C, Feusier G and de Rooij N F 2000 One mask nickel micro-fabricated reed relay *IEEE 13th Ann. Int. Conf. Micro Electro Mechanical Systems* pp 176–80
- [8] Simon J, Saffer S, Sherman F and Kim C-J 1998 Lateral polysilicon microrelays with a mercury microdrop contact *IEEE Trans. Indust. Electron.* **45** 854–60
- [9] Li Z, Zhang D, Li T, Wang W and Wu G 2000 Bulk micromachined relay with lateral contact *J. Micromech. Microeng.* **10** 329–33
- [10] Schiele I and Hillerich B 1999 Comparison of lateral and vertical switches for application as microrelays *J. Micromech. Microeng.* **9** 146–50
- [11] Tang M, Liu A-Q, Agarwal A, Zhang Q X and Win P 2004 A new approach of lateral RF MEMS switch *Analog Integr. Circuits Signal Process.* **40** 165–73
- [12] Tang M, Win P, Goh W L, Agarwal A, Law L C and Liu A-Q 2004 A single-pole double-throw (SPDT) circuit using deep etching lateral metal-contact switches *IEEE MTT-S Int. Microwave Symp. Digest* pp 581–4
- [13] Reyes A C, El-Ghazaly S M, Dorn S J, Dydyk M, Schroder D K and Patterson H 1995 Coplanar waveguides and microwave inductors on silicon substrates *IEEE Trans. Microw. Theory Tech.* **43** 2016–22
- [14] Tilmans H A C 2002 MEMS components for wireless communications *16th European Conf. Solid-State Trans.* pp 1–34
- [15] Pozar D M 1990 *Microwave Engineering* (Reading, MA: Addison-Wesley)
- [16] Gere J M and Timoshenko S P 1997 *Mechanics of Material* 4th edn (Boston, MA: PWS)
- [17] Burger G J, Smulders E J T, Berenschot J W, Lammerink T S J, Fluitman J H J and Imai S 1996 High-resolution shadow-mask patterning in deep holes and its application to an electrical wafer feed-through *Sensors Actuators A* **54** 669–73